Reconstructing 3D proton dose distribution using ionoacoustics

van Dongen, Koen; de Blécourt, Anne; Lens, Eelco; Schaart, Dennis; Vos, Frans

DOI
10.1088/1361-6560/ab4cd5

Publication date
2019

Document Version
Final published version

Published in
Physics in Medicine and Biology

Physics in Medicine & Biology

PAPER

Reconstructing 3D proton dose distribution using ionoacoustics

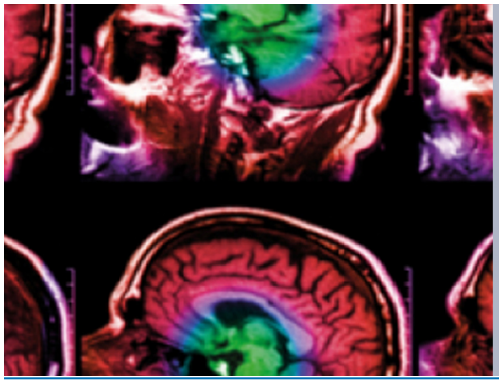

IOP Publishing Phys. Med. Biol. 64 (2019) 225005 (14pp) https://doi.org/10.1088/1361-6560/ab4cd5

Physics in Medicine & Biology

IPEM Institute of Physics and Engineering in Medicine

PAPER

Reconstructing 3D proton dose distribution using ionoacoustics

K W A van Dongen[1,3], A J de Blécourt[1], E Lens[2], D R Schaart[2] and F M Vos[1]

[1] Department of Imaging Physics, Faculty of Applied Sciences, Delft University of Technology, Delft, The Netherlands
[2] Department of Radiation Science & Technology, Faculty of Applied Sciences, Delft University of Technology, Delft, The Netherlands
[3] Author to whom correspondence should be addressed.

E-mail: k.w.a.vandongen@tudelft.nl

RECEIVED
24 April 2019

REVISED
1 October 2019

ACCEPTED FOR PUBLICATION
10 October 2019

PUBLISHED
15 November 2019

Keywords: 3D inversion, Bragg peak, proton range verification, ionoacoustics

Abstract

In proton therapy high energy protons are used to irradiate a tumor. Ideally, the delivered proton dose distribution is measured during treatment to ensure patient safety and treatment effectiveness. Here we investigate if we can use the ionoacoustic wave field to monitor the actual proton dose distribution for the two most commonly used proton accelerators; the isochronous cyclotron and the synchrocyclotron. To this end we model the acoustic field generated by the protons when irradiating a heterogeneous cancerous breast with a 89 MeV proton beam. To differentiate between the systems, idealized temporal micro-structures of the beams have been implemented. Results show that by employing model-based inversion we are able to reconstruct the 3D dose distributions from the simulated noisy pressure fields. Good results are obtained for both systems; the absolute error in the position of the maximum amplitude of the dose distribution is 5.0 mm for the isochronous cyclotron and 5.2 mm for the synchrocyclotron. In conclusion, this numerical study suggests that the ionoacoustic wave field may be used to monitor the proton dose distribution during breast cancer treatment.

1. Introduction

X-ray radiation therapy is an established method to treat patients suffering from cancer. Unfortunately, radiation toxicity is an important side effect which can dramatically affect quality-of-life of patients. Proton therapy is a relatively new form of radiotherapy during which tumors are irradiated with protons (instead of photons). A key advantage of proton therapy lies in the much more localized deposition of energy, thereby minimizing negative side effects. However, the sharp delineation of the treated area makes proton therapy susceptible to marginal misses, e.g. due to organ movement, changes in organ filling or patient weight (Unkelbach and Paganetti 2018). Currently, this problem is solved by applying a safety margin around the tumor, effectively irradiating more tissue than necessary.

Imaging the proton dose distribution in real time, during proton therapy, may be the key to alleviate the need for irradiating more tissue than actually required; knowing the actual delivered dose distribution could allow for adaptation of the irradiation plan during the treatment. Several methods of monitoring the proton dose distribution non-invasively and in real-time have spiked research interest. Among these methods are prompt gamma imaging (Min *et al* 2006), PET imaging (Parodi *et al* 2007, Parodi 2015), and ionoacoustic imaging (Hickling *et al* 2018). While each method has its own advantages and disadvantages, ionoacoustic imaging is unique in the sense that it uses relatively cheap and compact measurement devices. Consequently, it can be used at the irradiation gantry, with the patient fully aligned to the treatment system. Hence, ionoacoustic imaging potentially enables non-invasive and real-time monitoring with minimal logistical efforts.

Measurements of the ionoacoustic wave field were performed for the first time in 1979 (Sulak *et al* 1979). Later, the field was measured during the irradiation of a patient (Hayakawa *et al* 1995). Recently, it was shown that the Bragg peak location can be determined from acoustic measurements in homogeneous media (water) (Kellnberger *et al* 2016) using modified back-projection algorithms (Xu and Wang 2005). To improve on interpretation, an ultrasound image was co-registered with an ionoacoustic reconstruction of the Bragg peak loca-

tion in homogeneous media (water) using model based reconstruction methods (Rosenthal *et al* 2010) or for heterogeneous media using filtered back-projection (Patch *et al* 2016). Experiments using clinically relevant system settings have shown that sub-millimeter proton range verification in homogeneous media is feasible (Lehrack *et al* 2017). At the same time, a numerical study showed the feasibility of range verification in heterogeneous media based on the arrival times of the ionoacoustic wave field (Jones *et al* 2018). Experimentally, three-dimensional (3D) imaging of the proton Bragg peak has been performed in a mouse leg for low energy (20 MeV) protons (Kellnberger *et al* 2016) using modified back-projection algorithms (Xu and Wang 2005) and model-based reconstructions (Rosenthal *et al* 2010).

To improve on existing imaging methods, we present a new 3D reconstruction method that iteratively reconstructs the unknown proton dose distribution from the known measured pressure field. To regularize this inverse problem, the temporal profile of the applied proton beam is included as *a priori* knowledge in the applied scheme. As the temporal profile is accelerator specific, we will derive a frequency domain formulation for the temporal beam characteristics for the two most commonly used accelerators: the isochronous cyclotron and the synchrocyclotron. Synchrotrons have not been included in the current analysis as they are not used as frequently as the isochronous cyclotrons and synchrocyclotrons. To further improve on existing methods, we do our entire analysis in the frequency domain, as this has several advantages; (1) by using frequency domain Greens functions one may use a coarser grid to compute the wave field without losing accuracy; (2) to solve the inverse problem, one may consider to use only a few frequency components instead of the entire available bandwidth (Verweij *et al* 2014, van Dongen *et al* 2018). Both will lead to a reduction in computational load.

The layout of this article is as follows. In section 2, we describe the theory underlying the ionoacoustic wave field. Here we also present an expression for the temporal beam profile of each accelerator. In section 3, we define the forward and the inverse problem. In section 4, we discuss the spill duration optimization method, the noise model we used to contaminate our simulated data with noise, as well as the simulation configuration. Results are presented in section 5. Finally, in sections 6 and 7 the obtained results are discussed and conclusions are presented.

2. Theory

Ionoacoustics show many similarities with photo-acoustics and the tutorial by Wang (2008) is recommended as an introduction to the mathematics involved.

2.1. Acoustic source

Assuming that the duration of the proton pulse is short with respect to the thermal diffusion time, the absorbed dose rate $D(\mathbf{r}, t)$, i.e. the absorbed energy normalized by the mass density, results in a volume source density of injection rate $q(\mathbf{r}, t)$ according to Wang (2008)

$$q(\mathbf{r}, t) = \frac{\Gamma(\mathbf{r})}{\rho(\mathbf{r})\, c^2(\mathbf{r})} E(\mathbf{r}, t) = \frac{\Gamma(\mathbf{r})}{c^2(\mathbf{r})} D(\mathbf{r}, t), \tag{1}$$

where $\Gamma(\mathbf{r})$, $\rho(\mathbf{r})$ and $c(\mathbf{r})$ are the Grüneisen parameter, the mass density and the speed of sound of the medium, respectively, and $E(\mathbf{r}, t)$ is the deposited energy density per unit time as a function of the position $\mathbf{r}$ and time t.

In (1), the assumption is made that the proton energy deposited in the tissue is instantaneously converted to heat. Hence, the energy related to the formation and radiation of secondary particles as well as the time the protons need to travel through the tissue are neglected. The latter is evident given the observation that the protons move at nearly relativistic speeds.

For ionoacoustics, the absorbed dose rate $D(\mathbf{r}, t)$ and the source $q(\mathbf{r}, t)$ can be separated into two parts; the first part describes the spatial distribution and the second its temporal behavior, consequently

$$q(\mathbf{r}, t) = q_{\mathbf{r}}(\mathbf{r})\, q_t(t) = \frac{\Gamma(\mathbf{r})}{c^2(\mathbf{r})} D_{\mathbf{r}}(\mathbf{r})\, D_t(t). \tag{2}$$

To model the acoustic source and the propagation of the acoustic wave field in heterogeneous media we will use a frequency formulation. Transforming (2) to the frequency domain with angular frequency ω yields

$$\hat{q}(\mathbf{r}, \omega) = q_{\mathbf{r}}(\mathbf{r})\, \hat{q}_\omega(\omega) = \frac{\Gamma(\mathbf{r})}{c^2(\mathbf{r})} D_{\mathbf{r}}(\mathbf{r})\, \hat{D}_\omega(\omega), \tag{3}$$

where we use the caret symbol $\hat{\ }$ to mark quantities defined in the frequency domain.

2.2. Temporal pulse properties

To develop our theory we make several assumptions that are common in the field of iono- and photo-acoustics. They play a role in, amongst others things, the derivation of the expression for the Grüneisen parameter (Wang 2008). These assumptions are discussed below.

2.2.1. Thermal confinement

This assumption entails that the spill duration t_{spill} is shorter than the time it takes for heat to dissipate over the proton beam diameter d_{beam}. If this condition is not met, the acoustic source will 'diffuse' through space. The condition of thermal confinement is given by

$$t_{\text{spill}} < \frac{d_{\text{beam}}^2}{4\alpha_{\text{thermal}}}, \tag{4}$$

where α_{thermal} is the thermal diffusivity of the medium. For $d_{\text{beam}} = 15$ mm (a representative value at the Bragg peak (Schwaab *et al* 2011)) and $\alpha_{\text{thermal}} = 0.14$ mm^2 s^{-1} (Krumholz *et al* 2011), this assumption dictates that $t_{\text{spill}} < 4 \cdot 10^2$ s. Consequently, the condition of thermal confinement is always satisfied in proton therapy.

2.2.2. Stress confinement

The condition of stress confinement is met, if t_{spill} is shorter than the transfer time of the acoustic wave over the beam diameter d_{beam}, hence

$$t_{\text{spill}} < \frac{d_{\text{beam}}}{c_0}, \tag{5}$$

where c_0 denotes the speed of sound of the medium. For $d_{\text{beam}} = 15$ mm and $c_0 = 1500$ m s^{-1}, stress confinement requires that $t_{\text{spill}} < 10$ μs. Spot irradiation can take several tens of microseconds, depending on the applied beam current. Consequently, this condition is not always satisfied in proton therapy. Fortunately, stress confinement is not required in the case in which $D_t(t)$ is known and applied in the model as is done with the implementation for the current manuscript.

2.3. Accelerator types

The two most common types of particle accelerators used in proton therapy are the isochronous cyclotron and the synchrocyclotron. Both systems accelerate particles on a cyclic path for a number of revolutions. A magnetic field is used to constrain the particles in their cyclic path, while an electric field is used to accelerate them.

The protons in both the isochronous cyclotron and the synchrocyclotron follow a spiral path, of which the radius increases with the proton speed. Eventually the protons are ejected from the cyclotron when they have reached a certain energy.

The difference between isochronous cyclotrons and synchrocyclotrons lies in the way they deal with relativistic effects. Due to the relativistic speed of the protons they gain mass. Isochronous cyclotrons compensate for this by applying a radial gradient to the magnetic field that constrains the protons, while synchrocyclotrons decrease the accelerator frequency as the protons traverse the spiral. Therefore, a synchrocyclotron generates inherently a pulsed beam, while an isochronous cyclotron can provide a macroscopically[3] continuous beam.

During therapy, a proton pencil beam is pointed sequentially at a list of locations in the tumor. Each pencil beam contains a sequence of proton spills. The temporal profiles of the proton spills generated by these accelerators are shown in figure 1 and discussed below. The presented proton spills are normalized such that when $D_t(t)$ is integrated over time it is equal to one. In addition, the subscripts *ic* and *sc* refer to an isochronous cyclotron and a synchrocyclotron, respectively.

2.3.1. Isochronous cyclotron

An isochronous cyclotron emits a series of equally sized and spaced bunches of protons. A series of bunches grouped together form a proton spill. The temporal dependence of the proton spill is described by

$$D_{t,\text{ic}}(t) = \left(\sqrt{2\pi}\sigma_{t,ic}N_{\text{ic}}\right)^{-1} \sum_{n=0}^{N_{\text{ic}}-1} e^{-\frac{1}{2}[(t-n\tau_{\text{ic}})/\sigma_{t,\text{ic}}]^2}, \tag{6}$$

with $\sigma_{t,\text{ic}}$ the Gaussian width of the proton bunch, N_{ic} the number of proton bunches, and τ_{ic} the temporal spacing between successive proton bunches. In the frequency domain (6) equals

$$\begin{aligned}\hat{D}_{\omega,\text{ic}}(\omega) &= \left(\sqrt{2\pi}N_{\text{ic}}\right)^{-1} \sum_{n=0}^{N_{\text{ic}}-1} e^{-in\tau_{\text{ic}}\omega - \omega^2\sigma_{t,\text{ic}}^2/2} \\ &= \left(\sqrt{2\pi}N_{\text{ic}}\right)^{-1} \frac{1-e^{-i\omega\tau_{\text{ic}}N_{\text{ic}}}}{1-e^{-i\omega\tau_{\text{ic}}}} e^{\omega^2\sigma_{t,\text{ic}}^2/2},\end{aligned} \tag{7}$$

where we used the relation $\sum_{n=0}^{N-1} a^n = \frac{1-a^N}{1-a}$ with $a = e^{-i\omega\tau_{\text{ic}}}$.

[3] Here, we distinguish the microscopic scale of individual proton bunches (nanosecond scale) from the macroscopic scale of the proton spill (microsecond scale).

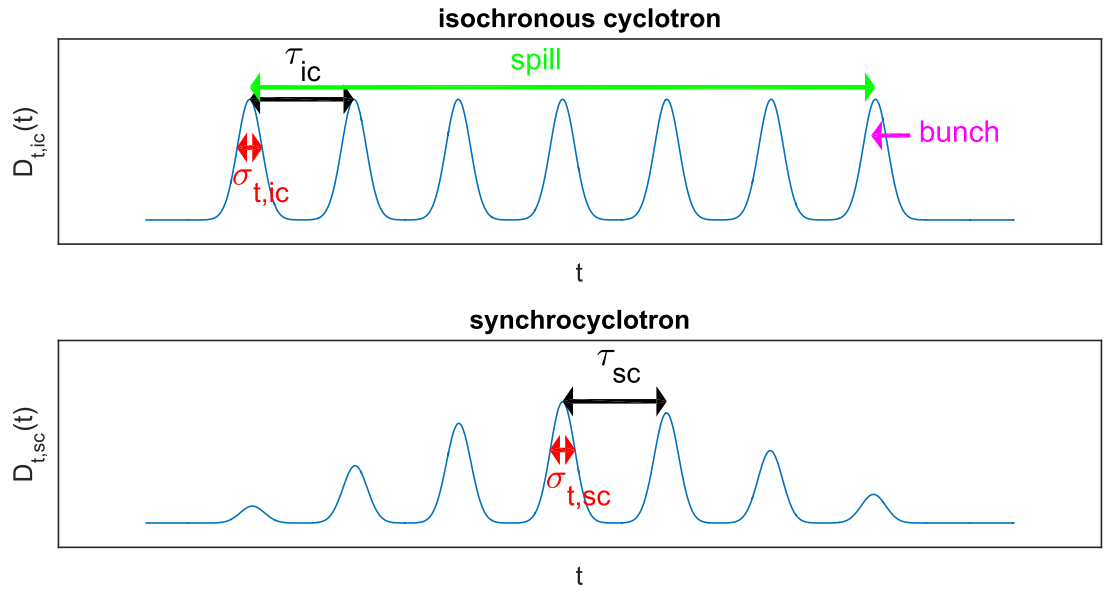

Figure 1. Temporal structures of the proton dose distributions generated by an (top) isochronous cyclotron and (bottom) synchrocyclotron. Dimensions are not to scale. The spills contain a series of bunches of width $\sigma_{t,ic}$ and $\sigma_{t,sc}$, respectively. Each bunch is separated by a time τ_{ic} and τ_{sc}, respectively.

The presented temporal dose distribution $D_{t,\mathrm{ic}}(t)$ represents the ideal situation; currently, the train of bunches cannot be turned on and off immediately and the envelope of the spill becomes more or less Gaussian. This can easily be included in the model as is done for the synchrocyclotron described in the next section. In the future, these sharp turn on and turn off times may be achieved by using a chopper (Patch *et al* 2016).

2.3.2. *Synchrocyclotron*

The temporal structure of the proton beam for a synchrocyclotron looks similar to the structure of a beam from an isochronous cyclotron, but multiplied with a Gaussian envelope of width σ_m that modulates the amplitude of the N_{sc} proton spills. The appendix contains the derivations for the results presented in this section. The temporal dependence of the proton dose is modeled by

$$D_{t,\mathrm{sc}}(t) = \left(\int_{-\infty}^{+\infty}\sum_{n=0}^{N_{\mathrm{sc}}-1} e^{-\frac{1}{2}\left[\left(\left[t'-n\tau_{\mathrm{sc}}\right]/\sigma_{t,\mathrm{sc}}\right)^2+\left(\left[t'-3\sigma_m\right]/\sigma_m\right)^2\right]}\mathrm{d}t'\right)^{-1} \sum_{n=0}^{N_{\mathrm{sc}}-1} e^{-\frac{1}{2}\left[\left(\left[t-n\tau_{\mathrm{sc}}\right]/\sigma_{t,\mathrm{sc}}\right)^2+\left(\left[t-3\sigma_m\right]/\sigma_m\right)^2\right]} \tag{8}$$

$$= \left(\sqrt{\frac{2\pi\sigma_{t,\mathrm{sc}}^2\sigma_m^2}{\sigma_{t,\mathrm{sc}}^2+\sigma_m^2}}\sum_{n=0}^{N_{\mathrm{sc}}-1} e^{-\left(n\tau_{\mathrm{sc}}-3\sigma_m\right)^2/2\left(\sigma_{t,\mathrm{sc}}^2+\sigma_m^2\right)}\right)^{-1} \sum_{n=0}^{N_{\mathrm{sc}}-1} e^{-\frac{1}{2}\left[\left(\left[t-n\tau_{\mathrm{sc}}\right]/\sigma_{t,\mathrm{sc}}\right)^2+\left(\left[t-3\sigma_m\right]/\sigma_m\right)^2\right]}. \tag{9}$$

Notice that each term contains two Gaussians: the first represents the individual proton bunches and the second the modulating function. In the frequency domain, this translates to

$$\hat{D}_{\omega,\mathrm{sc}}(\omega) = \left(\sqrt{2\pi}\sum_{n=0}^{N_{\mathrm{sc}}-1} e^{-\left(n\tau_{\mathrm{sc}}-3\sigma_m\right)^2/2\left(\sigma_{t,\mathrm{sc}}^2+\sigma_m^2\right)}\right)^{-1} \sum_{n=0}^{N_{\mathrm{sc}}-1} e^{-\frac{\left(\omega\sigma_{t,\mathrm{sc}}\sigma_m\right)^2+2i\omega\left(n\tau_{\mathrm{sc}}\sigma_m^2+3\sigma_m\sigma_{t,\mathrm{sc}}^2\right)+\left(n\tau_{\mathrm{sc}}-3\sigma_m\right)^2}{2\left(\sigma_{t,\mathrm{sc}}^2+\sigma_m^2\right)}}. \tag{10}$$

2.4. Acoustic wave field

The acoustic wave equation describing the pressure wave field $p_{\mathrm{tot}}(\mathbf{r},t)$ propagating in a lossless medium with a spatially varying speed of sound $c(\mathbf{r})$ and a constant volume density of mass reads

$$\left(\nabla^2 - \frac{1}{c^2(\mathbf{r})}\partial_t^2\right) p_{\text{tot}}(\mathbf{r},t) = -\rho_0 \partial_t q(\mathbf{r},t), \tag{11}$$

where the volume source density of injection rate $q(\mathbf{r},t)$ is induced by the protons interacting with the tissue and where ∂_t denotes the temporal derivative. Transforming (11) to the frequency domain yields

$$\left(\nabla^2 + \frac{\omega^2}{c_0^2}\right) \hat{p}_{\text{tot}}(\mathbf{r},\omega) = -i\omega\rho_0 \hat{q}(\mathbf{r},\omega) - \omega^2 \left(\frac{1}{c^2(\mathbf{r})} - \frac{1}{c_0^2}\right) \hat{p}_{\text{tot}}(\mathbf{r},\omega). \tag{12}$$

To solve (12) for $\hat{p}_{\text{tot}}(\mathbf{r},\omega)$, (12) is reformulated—without any approximation—into an integral equation formulation (Fokkema and van den Berg1993). With this formulation, the total pressure field $\hat{p}_{\text{tot}}(\mathbf{r},\omega)$ is described by the sum of an incident pressure field $\hat{p}_{\text{inc}}(\mathbf{r},\omega)$ and a scattered pressure field $\hat{p}_{\text{sct}}(\mathbf{r},\omega)$, hence

$$\hat{p}_{\text{tot}}(\mathbf{r},\omega) = \hat{p}_{\text{inc}}(\mathbf{r},\omega) + \hat{p}_{\text{sct}}(\mathbf{r},\omega), \tag{13}$$

with

$$\hat{p}_{\text{inc}}(\mathbf{r},\omega) = i\omega\rho_0 \hat{q}_\omega(\omega) \int_{\mathbf{r}'\in\mathbb{D}} \hat{G}(\mathbf{r}-\mathbf{r}',\omega)\, q_{\mathbf{r}}(\mathbf{r}')\, \mathrm{d}V(\mathbf{r}'), \tag{14}$$

$$\hat{p}_{\text{sct}}(\mathbf{r},\omega) = \omega^2 \int_{\mathbf{r}'\in\mathbb{D}} \hat{G}(\mathbf{r}-\mathbf{r}',\omega)\, \chi(\mathbf{r}') \hat{p}_{\text{tot}}(\mathbf{r}',\omega)\, \mathrm{d}V(\mathbf{r}'), \tag{15}$$

where heterogeneities in the speed of sound are accounted for via the contrast function

$$\chi(\mathbf{r}') = \frac{1}{c^2(\mathbf{r}')} - \frac{1}{c_0^2}, \tag{16}$$

and where the frequency-domain Green's function, i.e. the impulse response of the embedding, reads

$$\hat{G}(\mathbf{r}-\mathbf{r}',\omega) = \frac{e^{-i\frac{\omega}{c_0}|\mathbf{r}-\mathbf{r}'|}}{4\pi|\mathbf{r}-\mathbf{r}'|}. \tag{17}$$

The spatial convolutions in (14) and (15) are taken over the spatial domain $\mathbb{D}$, i.e. the regions where the absorbed dose rate described via the source term $\hat{q}(\mathbf{r},\omega)$ and / or the contrast function $\chi(\mathbf{r}')$ are non-zero. Hence, $\hat{p}_{\text{inc}}(\mathbf{r},\omega)$ is the field generated by the primary sources and the scattered field $\hat{p}_{\text{sct}}(\mathbf{r},\omega)$ may be seen as a correction term to the incident field to yield the total field $\hat{p}_{\text{tot}}(\mathbf{r},\omega)$. With this formulation, multiple scattering and phase shifts induced by a spatially varying speed of sound are accounted for whereas scattering induced by a spatially varying mass density is neglected; a commonly made approximation in the field of medical ultrasound (Taskin *et al* 2018).

3. Forward and inverse model

3.1. Forward problem

Acoustic wave propagation is modeled using a full-wave modeling technique that accounts for (multiple) scattering as well as phase shifts in the propagating wave field due to heterogeneities in the acoustic medium properties (Ozmen-Eryilmaz *et al* 2011, Verweij *et al* 2014, Taskin *et al* 2018). The employed method solves (13)–(16) for heterogeneous lossless media. Absorption is assumed to be negligible due to the low frequencies involved (Taskin *et al* 2018).

To solve the forward problem we took into account a spatially varying mass density when computing the spatial dose distribution $D(\mathbf{r},t)$. However, when computing the acoustic source $q(\mathbf{r},t)$ from $D(\mathbf{r},t)$ according to (3), we assumed the medium to be homogeneous. This is due to the fact that for all the individual breast tissues the corresponding Grüneisen parameters are not always known. Finally, to compute the resulting wave field (including multiple scattering and phase shifts), we assumed the medium to be heterogeneous again. Hence, we only assumed the medium to be homogenous in (3), when computing $q(\mathbf{r},t)$ from $D(\mathbf{r},t)$.

3.2. Inverse problem

To reconstruct the spatial dose distribution $D_{\mathbf{r}}(\mathbf{r})$, i.e. the dose $D(\mathbf{r},t)$ integrated over time, a model based inversion method is employed. The employed inversion model is based on the Born approximation, asserting that the (multiple) scattering of the acoustic wave is negligible. This approximation is valid due to the low frequency content of the ionoacoustic wavefield (Taskin *et al* 2018). Consequently, for imaging, (13) reduces to $\hat{p}_{\text{tot}}(\mathbf{r}^R,\omega) = \hat{p}_{\text{inc}}(\mathbf{r}^R,\omega)$ with $\mathbf{r}^R$ the position of receiver R.

To reconstruct the unknown dose distribution $D_{\mathbf{r}}(\mathbf{r})$ from the field measured by receiver R, denoted as $\hat{p}_{\text{meas}}(\mathbf{r}^R,\omega)$, a conjugate gradient minimization scheme is used to minimize the L2-norm based cost functional

$$E = ||\hat{p}_{\text{meas}}(\mathbf{r}^R,\omega) - \hat{p}_{\text{inc}}(\mathbf{r}^R,\omega)||^2 \tag{18}$$

for the unknown dose distribution $D_{\mathbf{r}}(\mathbf{r})$, where $\hat{p}_{\text{inc}}(\mathbf{r}^R, \omega)$ is computed via (14). Here, we take the initial dose distribution to be zero everywhere; clearly, in practice one could use the dose distribution coming from the treatment planning as starting model to reduce computing time and/or to reduce the domain of interest to the non-zero dose region only. Note that the known temporal shape of the absorbed dose rate, $D_\omega(\omega)$, is included as *a priori* knowledge in the inversion scheme. To reduce computational time, only a limited number of frequency components may be used during inversion.

4. Methods

4.1. Spill duration optimization

For a given treatment, the prescribed dose and hence the total number of protons is set by the treatment plan. However, there is a degree of freedom in how this dose is distributed over time. In this work we use this degree of freedom to maximize the amplitude of the pressure field for the isochronous cyclotron only, as the synchrocyclotron has a fixed spill time.

The delivered dose is attained by integrating the proton beam current I_{proton} over the total beam time t_{beam}. Preferably, the current is set to its maximum allowable value to maximize the amplitude of the acoustic wave field. Meanwhile, the required beam time may be expressed as $t_{\text{beam}} = N_{\text{rep}} \times t_{\text{spill}}$, with N_{rep} the number of proton spills of length t_{spill}. Essentially, when successive spills are well separated in time each individual proton spill corresponds to a single acoustic measurement; i.e. the wave fields generated by the individual proton spills should not overlap in time, hence the time between two successive spills should be at least in the order of 0.2 ms. From the theory presented in section 2 (see e.g. equations (2) and (11)), it can be concluded that the amplitude of the pressure field is a function of the dose distribution $D_t(t)$ and hence from t_{spill}. Consequently, the signal to noise ratio (SNR) is approximately equal to

$$SNR = \sqrt{N_{\text{rep}}} \frac{A_{\text{pres}}\left(t_{\text{spill}}\right)}{A_{\text{noise}}}, \tag{19}$$

where $A_{\text{pres}}(t_{\text{spill}})$ is the amplitude of the pressure field measured by the receivers, and A_{noise} is the amplitude of the noise in a single measurement.

For short spill durations ($t_{\text{spill}} \ll 1/f_0$, with f_0 the center or dominant frequency of the acoustic wave field), the temporal shape of the dose distribution can be approximated by a Dirac pulse $\delta(t)$. In this regime, longer spill durations give rise to an increase of the amplitude of the measured signal, since the deposited dose scales linearly with the spill duration. For very long spill durations, however, the acoustic wave starts to propagate over a significant distance during the dose deposition. This implies that, with increasing spill duration, the acoustic pulse gets wider in time instead of higher in amplitude. Consequently, $A_{\text{pres}}(t_{\text{spill}})$ will initially increase and later decrease with increasing t_{spill} (Jones *et al* 2016). Therefore, an optimal t_{spill} exists, where the SNR is maximal.

4.2. Noise model

Thermal medium noise is expected to influence the measurements. This type of noise is incorporated in the acoustic model according to Readhead (2014)

$$\langle p_i^2 \rangle = \frac{2k_B T \rho_0 c_0}{\pi^2 a^2} \left(1 - \frac{J_1(2k_i a)}{k_i a}\right) \mathrm{d}\omega, \tag{20}$$

where the value $\langle p_i^2 \rangle$ is the average square noise pressure in an angular frequency band of width $\mathrm{d}\omega$, centered at ω_i and averaged over the active surface of the transducer with radius a. In (20), k_B is the Boltzmann constant, J_1 is a first order Bessel function, $k_i = \omega_i / c_0$ is the wave number corresponding to angular frequency ω_i, and T is the temperature (310 K).

The total noise $p_{\text{noise}}(t)$ is modeled by taking multiple frequency bands, hence

$$\begin{aligned} p_{\text{noise}}(t) &= \sum_{\omega_i=\omega_{\min}}^{\omega_{\max}} \sqrt{2} \sin(\omega_i t + \phi_i) \sqrt{\langle p_i^2 \rangle} \\ &= \sum_{\omega_i=\omega_{\min}}^{\omega_{\max}} \sin(\omega_i t + \phi_i) \sqrt{\frac{4k_B T \rho_0 c_0}{\pi^2 a^2} \left(1 - \frac{J_1(2k_i a)}{k_i a}\right) \mathrm{d}\omega}, \end{aligned} \tag{21}$$

where $0 \leqslant \phi_i < 2\pi$ represents a random phase shift and t is time. The additional factor $\sqrt{2}$ is added to account for the fact that $\sqrt{\langle p_i^2 \rangle}$ is the root-mean-square value, which is related to the amplitude via the relation $p_{\text{peak}} = \sqrt{2}\, p_{\text{RMS}}$ for sinusoidal waves.

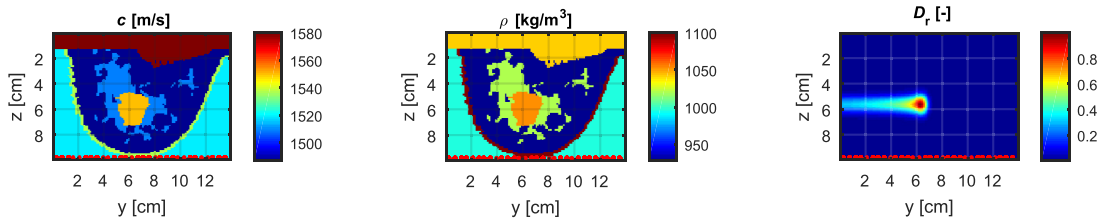

Figure 2. Cross-sections of the 3D breast model asserting different medium parameters and proton dose distribution: (left) speed of sound in $\mathrm{m\ s^{-1}}$, (middle) mass density in $\mathrm{kg\ m^{-3}}$, and (right) normalized proton dose for an isochronous cyclotron. Note that the breast is submerged in water. The model includes the following tissue types with their respective colors in the speed of sound image: water (light blue), muscle (brown), fat (dark blue), glandular tissue (purple), tumor (orange), and skin (green). The dose distributions for the other accelerator types look slightly narrower due to a lower initial beam width $\sigma_{r,i}$. The cross-sections are taken through the target voxel. The location of the receivers are marked by the red dots in the plane $z = 9.8$ cm.

4.3. Simulation configurations

The acoustic wave field is computed for a 3D breast phantom immersed in water (Bakker *et al* 2019) (see figure 2). The phantom is retrieved from an MRI scan of a cancerous breast and submerged in water to optimize the contact between the receivers and the breast. The phantom contains tissue-dependent information on the speed of sound and the mass density, and is discretised in cubic elements of size 1.235 mm in all directions. To obtain the simulated measurements, an ultrasound matrix transducer of 30 by 30 elements is modeled in the plane $z = 9.8$ cm. The point receivers are homogeneously distributed over the entire plane. To compute the noise, we assumed the elements to be submerged in water and to be of finite size with radius $a = 3$ mm. The Grüneisen parameter $\Gamma(\mathbf{r})$ is taken constant, at a value of $\Gamma_0 = 0.8$ (Yao *et al* 2014).

The proton irradiation is modeled for each accelerator type using the parameters presented in table 1. The Bragg peak is positioned in the center of the tumor, using a proton energy of 89 MeV, see figure 2. This coincides with a absorbed radiation dose in the Bragg peak region of approximately 1.2 Gy and a proton range of 63 mm in water (NIST 2018).

The spatial dose distribution is modeled using a pencil beam algorithm (Bortfeld 1997) with the beam axis taken parallel to the y-axis. The algorithm accounts for spatially varying mass density along the beam path. The lateral scattering is assumed to depend on the water equivalent depth, with a radial Gaussian of width

$$\sigma_r^2(y) = \sigma_{r,i}^2 + \left[0.0333R\left(0.1816\frac{\tilde{y}(y)}{R} + 0.8184\left[\frac{\tilde{y}(y)}{R}\right]^2\right)\right]^2, \tag{22}$$

where $\sigma_r(y)$ is the Gaussian width of the proton beam as a function of depth y, with the water equivalent depth $\tilde{y}(y) = \int_0^y \frac{\rho(u)}{\rho_0}\mathrm{d}u$. R is the effective proton range in water. The initial value $\sigma_{r,i} = \sigma_r(y = 0)$ depends on the beam delivery system.

Spill duration optimization is only applied to isochronous cyclotrons. Synchrocyclotrons have a fixed spill duration. To find the optimal spill duration, the pressure field is computed for a range of spill durations. Next, the spill duration corresponding to the pressure field with the highest SNR is selected for the numerical study. To reduce computing time, a homogeneous medium is used for the spill optimization. The receivers for determining the optimum spill duration are virtually placed on a ring around the point where the proton beam enters the tissue. The ring has a radius of half the proton range in water.

5. Results

5.1. Forward problem

To compute synthetic data, the forward problem is solved. Snapshots of the simulated noise-free wave fields are shown in figure 3. The displayed snapshots are shown in the same plane as used in figure 2. These results clearly show that the amplitudes of the scattered wave fields p_{sct} are much smaller than the amplitudes of the incident wave fields p_{inc} . Here the incident field represents the field generated by the protons interacting with water only (in absence of the breast). This is plausible since little scattering occurs at these low frequencies, see figure 4. The latter figure also clearly shows that the frequencies used for the inversion are well below 100 kHz. Figure 5 shows the frequency spectra for all the measurements for both systems. The results show that similar but not identical signals are obtained for both accelerators; the bandwidth of the ionoacoustic wavefield is slightly narrower for the isochronous cyclotron as compared to the synchrocyclotron. This may also be observed from the time domain signal in figure 5. These variations are due to spatial variations in the proton dose distributions as well as due to

Table 1. Beam parameters. The isochronous cyclotron model is based on the accelerator at HollandPTC (Delft, the Netherlands) which operates a Varian ProBeam device. The synchrocyclotron model is derived from the IBA S2C2 synchrocyclotron of CAL (Nice, France) as used in Lehrack *et al* (2017). Proton current values are averaged over the spill duration for the isochronous cyclotron and for the synchrocyclotron over one frequency sweep (Lehrack *et al* 2017, pulse repetition rate, p L27). The reported values are obtained from the following references: Jones *et al* (2015) denoted by (ic1) and Lehrack *et al* (2017) by (cs1).

Variable	Isochronous cyclotron	Synchrocyclotron
σ_t (ns)	$1^{(ic1)}$	$1^{(ic1)b}$
τ (ns)	13^{b}	$16^{(cs1)}$
σ_m (μs)	—	$2^{(cs1)a}$
σ_s (ns)	—	—
I_{proton} (nA)	$30^{(ic1)a}$	$2^{(cs1)}$
$\sigma_{r,i}$ (mm)	4.5^{b}	$3.2^{(cs1)a}$
$\tau_{spill,opt}$ (μs)	6.4^{b}	—
spill repetition rate (kHz)	—	$1^{(cs1)}$
$N_{protons}$ ($\times 10^8$)	5	5
N_{rep}	417	40

[a] quantity that is similar but not identical to the value mentioned in the reference.
[b] constructed or assumed value.
Note. $N_{protons}$ is taken as a fixed value and N_{rep} is computed such that the absorbed dose rate for both systems is identical.

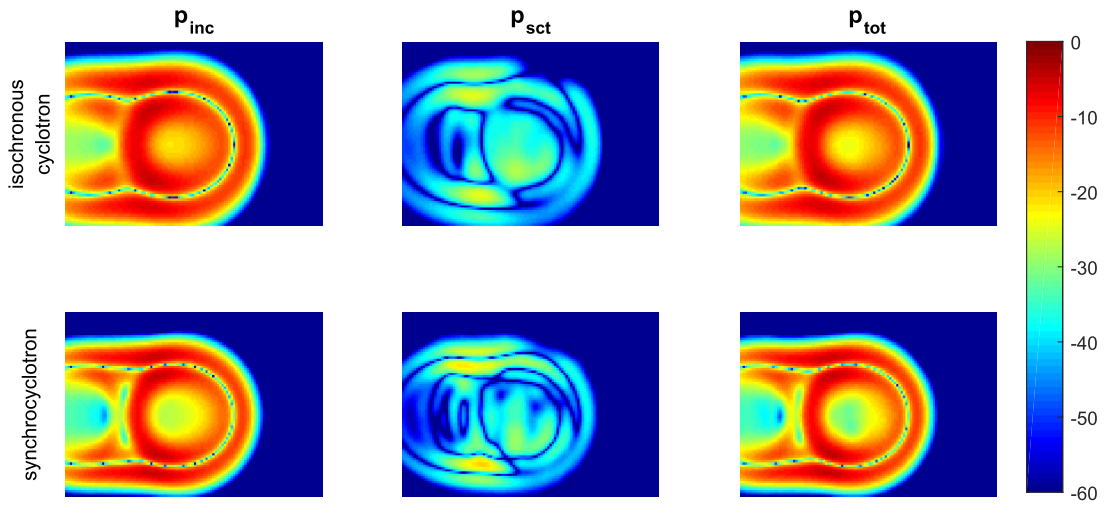

Figure 3. Snapshot at $t = 25$ μs of the noise-free wave fields for the isochronous cyclotron (top) and synchrocyclotron (bottom). From left to right: incident, scattered and total field. For each accelerator type, the fields are normalized with respect to the corresponding incident field. The color bar is on a dB scale. Note that the amplitude of the scattered field is at least 18 dB smaller than the amplitude of the incident field, hence scattering effects can be neglected.

variations in the temporal (micro-)structure of the beam. Figure 6 shows that the effective noise amplitude[4] is considerable. The RMS noise amplitude for a single measurement is 7.1 mPa, using $f_{max} = 200$ kHz.

The presented dose distribution in figure 1 for the isochronous cyclotron represents the ideal situation and may be achieved by including a chopper in the beam. This principle has been demonstrated for low energy (50 MeV) proton beams (Patch *et al* 2016) but not yet for the high energies that would be required for the current application. In the absence of such a chopper, the turn on and turn off times may be larger than 10 μs leading to a lower amplitude for the resulting acoustic wave field.

5.2. Inverse problem

After the forward problem is solved, the inverse problem is directed by reconstructing the proton dose distribution from the synthetically measured ionoacoustic wave field. To reduce computational time, only a subset of frequencies is used in the inversion process. Here all 32 frequencies in the range from 7 up to 77 kHz have been used (see also figure 4).

[4] This is the noise amplitude after averaging over a number of proton spills.

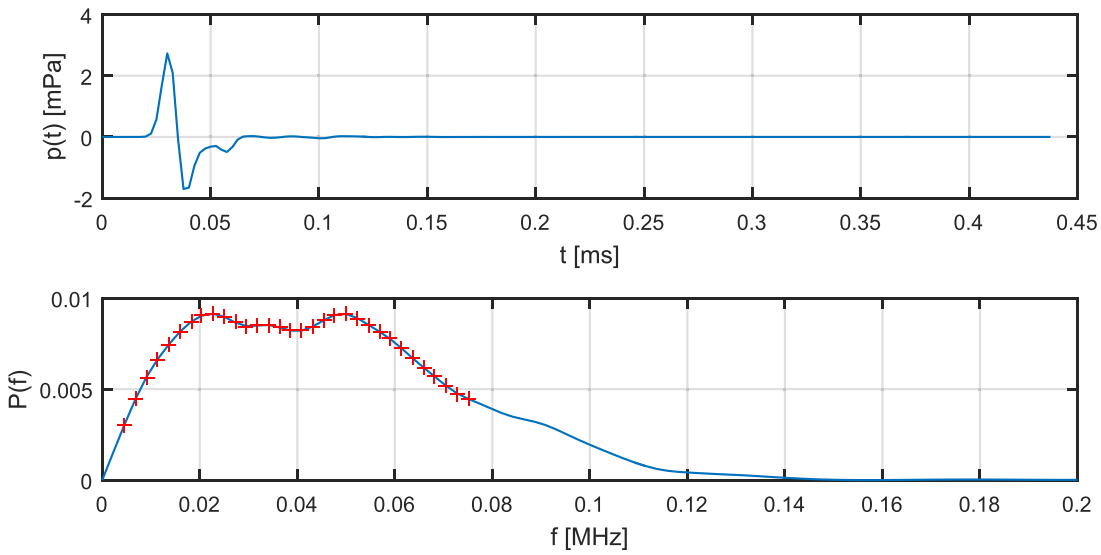

Figure 4. Typical noise-free A-scan for the isochronous cyclotron model in (top) time and (bottom) frequency domain. The A-scan is taken in the center of the plane $y = 0$.

5.2.1. 3D dose

Surface plots of the reconstructed dose are shown in figure 7. The displayed reconstructions correspond to the three orthogonal planes through the voxel with the highest (reconstructed) dose. A white marker is used to denote the location corresponding to the maximum of the original dose. In all cases, the inversion algorithm ran for eight iterations; for a higher number of iterations the reconstruction started to degrade due to a poor SNR.

To express the error in the reconstruction, we computed the offset in the location of the maximum of the reconstructed dose with respect to the location of the maximum of the original dose. The resulting offsets are denoted by E_x^{dose}, E_y^{dose} and E_z^{dose} for the x, y and z-direction, respectively, and displayed in table 2. The same procedure is followed for the integral depth dose (IDD) along the y-axis (E^{IDD}).

Finally, from results not shown it has been concluded that the maximum amplitude of the reconstructed dose is lower than the original amplitude.

5.2.2. Integral depth dose (IDD)

Comparing the IDD of the original dose and the reconstructed dose (see figure 8 and table 2) shows that the peak of the reconstructed IDD lies slightly less deep in the tissue and is also less sharp. In addition, from results not shown it is concluded that the amplitude of the reconstructed IDD is higher than the amplitude of the original IDD. This may be (partially) explained by the noise present in the data; as noise adds energy to the medium, the total source term becomes larger, resulting in a higher proton dose across the entire volume.

6. Discussion

The noise model employed in this research only concerns thermal medium noise. In a realistic measurement setup, other noise sources may apply and it is not given that thermal medium noise will be the dominant factor. Other research indicates that transducer noise may dominate thermal medium noise, depending on the transducer type (Oraevsky and Karabutov 2000, Winkler *et al* 2013, Ahmad *et al* 2015).

The authors have allowed themselves some liberty in estimating certain system parameters, most notable are the beam current for the isochronous cyclotron and the number of protons used in irradiation. It is highly desirable from an ionoacoustic point of view to set these values as high as possible, as they both affect the SNR greatly. Currently, however, beam currents are limited to fairly low levels; the isochronous cyclotron current, for example, is on the order of a few nA in current commercial therapy systems.

There is nevertheless a trend towards higher beam currents. Amongst others this is motivated by a desire to reduce dose blurring and interplay effects in the treatment of moving tumors, as well as by economical considerations (throughput). Moreover, recently published preclinical studies indicate that the use of ultrahigh dose rates may reduce normal-tissue damage (Favaudon *et al* 2014). The resulting trend towards higher proton beam currents is favorable for the potential of ionoacoustic range verification.

In our models we included the fine detailed temporal structure of each proton beam. This detailed structure has a temporal period well below the stress confinement time of approximately 1 μs, i.e. $\sigma_{t,ic} + \tau_{ic} \approx 14$ ns and

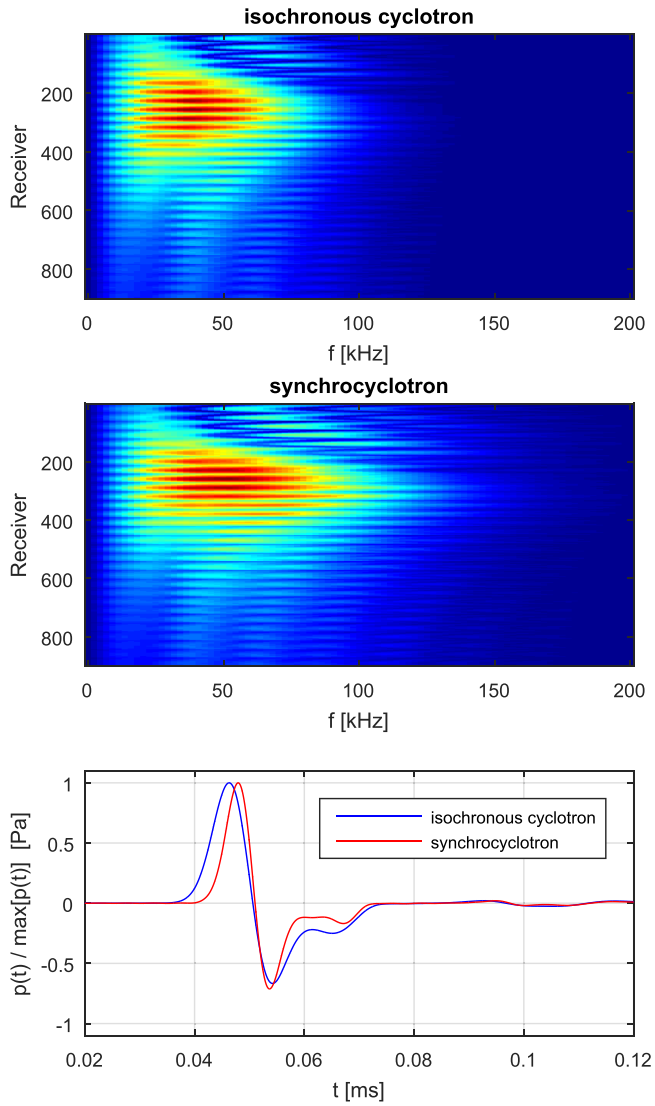

Figure 5. Frequency spectra for all measured A-scans corresponding to the accelerator types; (top) isochronous cyclotron and (middle) synchrocyclotron. (bottom) The A-scans are measured by a receiver located in the center of the plane $z = 9.8$ cm for both accelerator types. The spectrum of the wavefield generated by the protons from the synchrocyclotron is slightly broader than the spectrum corresponding to the isochronous cyclotron.

$\sigma_{t,sc} + \tau_{sc} \approx 17$ ns. Consequently, to simplify the temporal structures of the beam, one could approximate the resulting current via the normalized envelope of the fine detailed temporal structure of the proton beam, where the normalization is done such that the resulting proton dose remains the same. However, in case the spot size is too small ($d_{\text{beam}} < 1.5$ μm) for stress confinement to be satisfied, the above approximation is not applicable and the micro-structure of the beam, i.e. $D(t)$, needs to be taken into account.

The beam parameters for the two presented systems are based on ideal circumstances. These parameters and the microscopic temporal structure of the beam may vary between existing systems of the same accelerator type. For instance, the ideal chopper does not exist; in reality there will still be a finite rise time for the proton beam current. Consequently, when employing the presented method on real measured data it is important to incorporate the parameter values for the corresponding system.

With the current setup we aimed to achieve a 3D reconstruction of the proton dose distribution. To this end we placed the transducers in a plane parallel to the beam. However, in case one is mainly interested in the proton range or IDD, it might be better to place the receivers in the plane perpendicular to the beam direction as this will probably yield more accurate results. This idea is supported by the results presented in table 2 and figures 7 and 8. These results show that the error in the localization of the maximum dose is highest in the y-direction, which is also the direction of the proton beam, and smaller in the z-direction, which is perpendicular to the measurement plane.

The maximum amplitudes for the reconstructed doses are underestimated by 79% and 86% for the isochronous cyclotron and the synchrocyclotron, respectively. This is due to the spreading of the energy over a stretched beam profile. The maximum amplitudes for the reconstructed IDD doses are overestimated by 37% and 47%

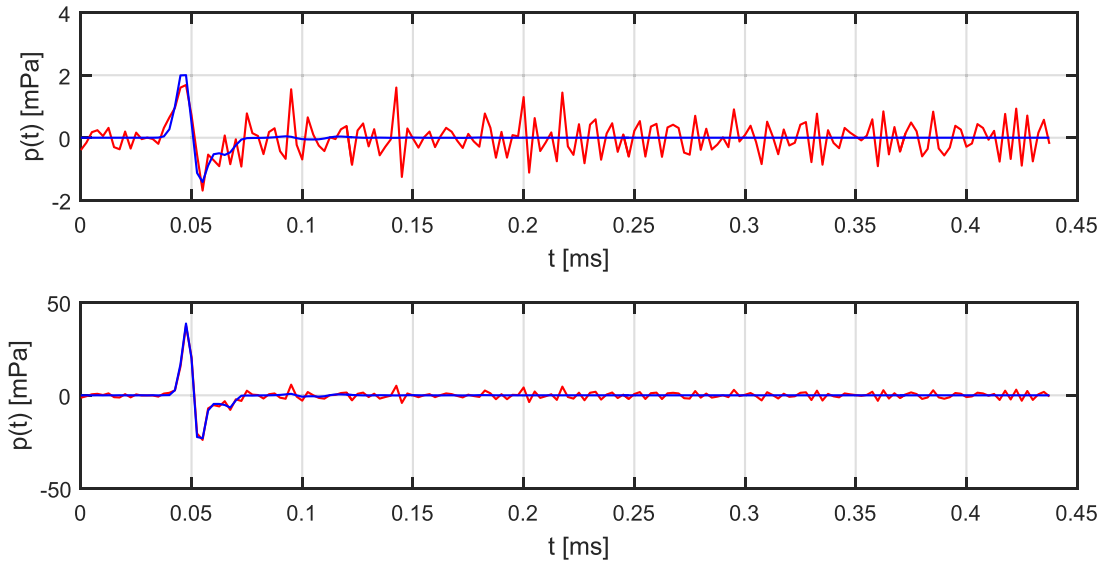

Figure 6. Typical A-scans corresponding to each accelerator; (top) isochronous cyclotron and (bottom) synchrocyclotron. The A-scans are measured by a receiver located in the center of the plane $z = 9.8$ cm. The red line shows the total signal including noise, while the blue line shows the noise-free signal. The noise amplitude used in these plots is the effective noise amplitude after averaging over a number of measurements (see table 1).

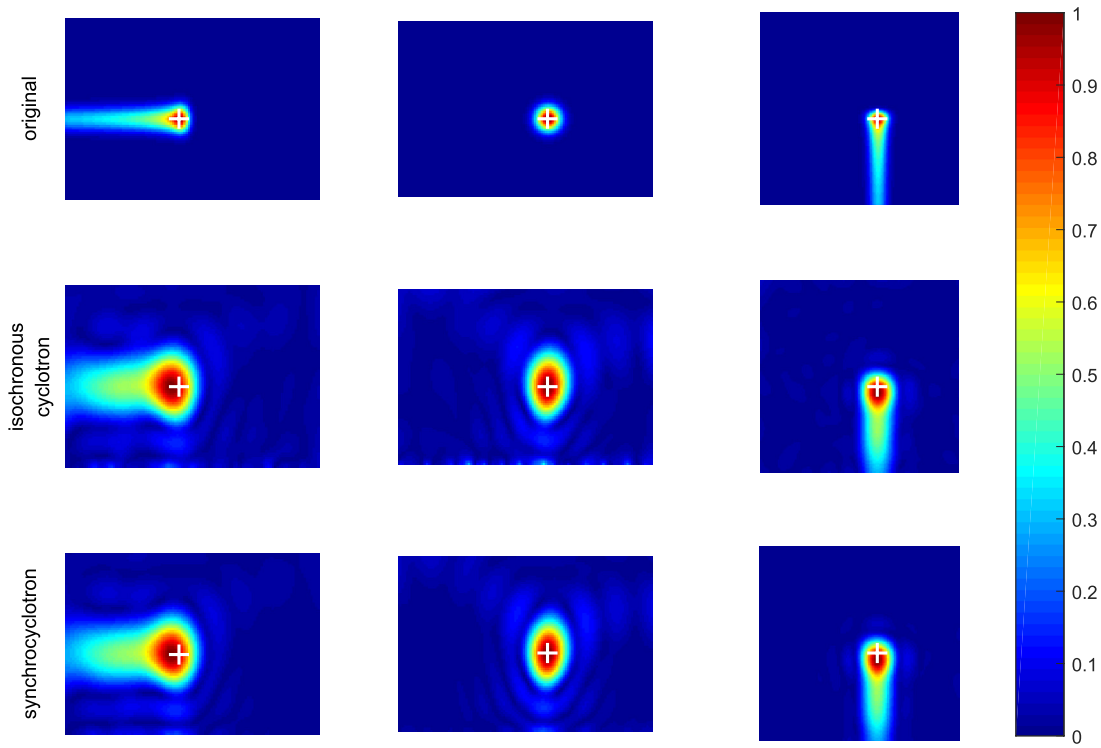

Figure 7. Cross sections of the reconstructed normalized doses, through the point of maximum dose. From top to bottom: original dose (isochronous cyclotron), isochronous cyclotron and synchrocyclotron. From left to right: (y, z)-plane, (x, z)-plane, (x, y)-plane. The reconstructions are based on 8 iterations. The white marker $(+)$ denotes the location with the highest original dose.

for the isochronous cyclotron and the synchrocyclotron, respectively. This is due to the noise present in the signal; this noise represents energy and hence leads to an overestimation of the delivered IDD. For all cases, the maximum in the reconstructed dose or IDD is positioned before and hence at a shallower depth than the original maximum. Why this is the case is not well understood and might be related to the receiver locations as well as to the low frequency content of the acoustic wave field. In many published experimental manuscripts, the configurations had been optimized to maximize the SNR and hence to reduce the effect of noise, whereas we tried to resemble a clinically realistic configuration.

Table 2. Reconstruction errors. The error in the localization of the maximum dose (E^{dose}) and of the maximum in the IDD (E^{IDD}), both with respect to the original dose distribution.

Variable	Isochronous cyclotron	Synchrocyclotron
E_x^{dose} (cm)	0.00	0.00
E_y^{dose} (cm)	0.50	0.37
E_z^{dose} (cm)	0.00	0.37
E^{IDD} (cm)	0.62	0.50

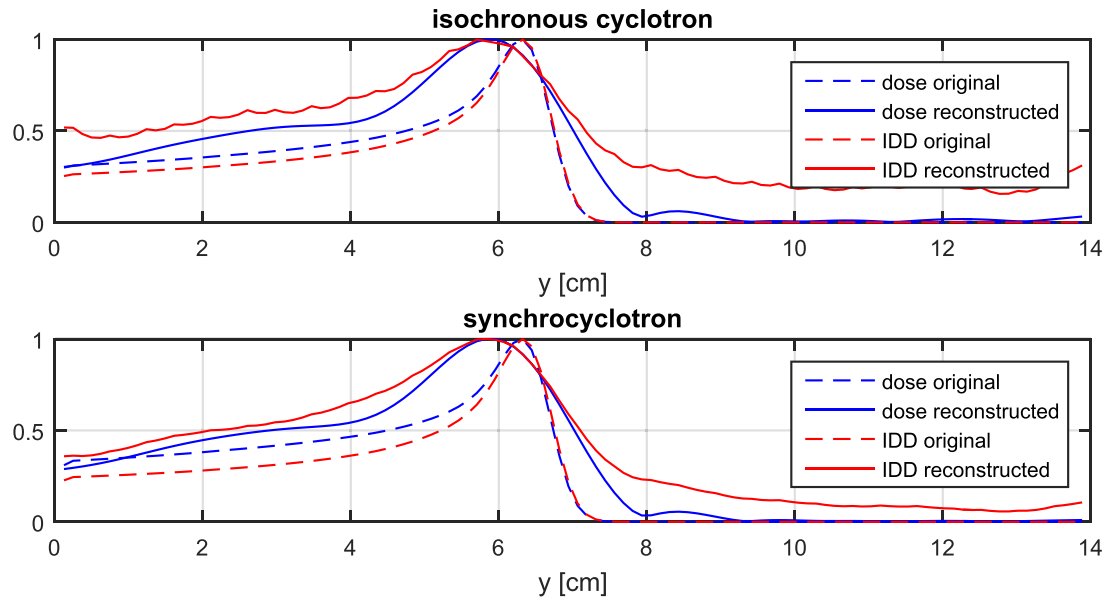

Figure 8. Dose (blue lines) and IDD (red lines) plots for the original (dashed lines) and reconstructed (solid lines) dose for (top) isochronous cyclotron and (bottom) synchrocyclotron. The results are normalized to one. The original/reconstructed dose and the IDD are taken parallel to y-axis, where the curves related the original/reconstructed dose are obtained along the straight through the voxel with the highest original/reconstructed dose.

Finally, solving the forward problem takes approximately 30 min; solving the inverse problem approximately one hour for eight iterations. However, care has to be taken with these numbers as the resulting times strongly depend on the computer and the implementation of the code (both have not been optimized to reduce computing time). Moreover, a good indication of the proton dose distribution is already obtained after one iteration. To reduce computing times, one may also consider to reduce the volume of interest to the region with non-zero dose rate or contrast (van Dongen *et al* 2007) or to limit the number of frequencies (van Dongen *et al* 2018).

7. Conclusion

Based on our numerical study it may be concluded that three-dimensional dose reconstruction using the ionoacoustic wave field is feasible for different accelerators used for proton therapy (isochronous cyclotron and synchrocyclotron). For the reconstruction we only used a few frequencies. To regularize the inverse problem we took advantage of the prior knowledge we have about the temporal micro-structure of the proton beam. The results also show that the inversion may be done within the Born approximation. The best results are obtained for the isochronous cyclotron, with the maximum dose location accurate within 5 mm. The obtained results suggest that by placing the receivers in a plane perpendicular to the beam direction (instead of parallel to the beam) the error in the beam direction may become smaller.

Acknowledgment

The authors express their gratitude to Prof. Dr. Katia Parodi and Dr. Walter Assmann of LMU Munich, for their willingness to share their experience to accelerate our research.

Appendix. Derivation of $D_{\omega,\text{sc}}(\omega)$

Equation (8) can be written as

$$D_{t,\mathrm{sc}}(t) = K^{-1}\sum_{n=1}^{N_{s,\mathrm{sc}}} e^{-\beta(t)/2}, \tag{A.1}$$

where

$$\beta(t) = \left(\frac{t - n\tau_{\mathrm{sc}}}{\sigma_{t,\mathrm{sc}}}\right)^2 + \left(\frac{t - 3\sigma_m}{\sigma_m}\right)^2 \tag{A.2}$$

and the normalization factor K reads

$$K = \int_{-\infty}^{+\infty}\sum_{n=1}^{N_{s,\mathrm{sc}}} e^{-\beta(t')/2}\mathrm{d}t'. \tag{A.3}$$

Expanding the terms and substituting

$$\sigma_{tm}^2 = \frac{\sigma_{t,\mathrm{sc}}^2\sigma_m^2}{\sigma_{t,\mathrm{sc}}^2 + \sigma_m^2} \tag{A.4}$$

and

$$\mu_{tm} = \frac{n\tau_{\mathrm{sc}}\sigma_m^2 + 3\sigma_m\sigma_{t,\mathrm{sc}}^2}{\sigma_{t,\mathrm{sc}}^2 + \sigma_m^2}, \tag{A.5}$$

equation (A.2) can be rewritten as (Bromiley 2018)

$$\beta(t) = \frac{(t - \mu_{tm})^2}{\sigma_{tm}^2} + \frac{(n\tau_{\mathrm{sc}} - 3\sigma_m)^2}{\sigma_{t,\mathrm{sc}}^2 + \sigma_m^2}. \tag{A.6}$$

Inserting (A.6) into (A.1) yields

$$D_{t,\mathrm{sc}}(t) = K^{-1}\sum_{n=1}^{N_{s,\mathrm{sc}}-1} e^{-(t-\mu_{tm})^2/2\sigma_{tm}^2} e^{-(n\tau_{\mathrm{sc}}-3\sigma_m)^2/2\left(\sigma_{t,\mathrm{sc}}^2+\sigma_m^2\right)}. \tag{A.7}$$

Note that the first exponential in (A.7) is a Gaussian, of which the Fourier transform has a known analytical solution. The second exponential in (A.7) does not depend on time and can thus be ignored in the Fourier transform. The frequency domain solution of (A.7) then becomes

$$D_{\omega,\mathrm{sc}}(\omega) = K^{-1}\sigma_{tm}\sum_{n=1}^{N_{s,\mathrm{sc}}-1} e^{-\omega^2\sigma_{tm}^2/2 - i\mu_{tm}\omega - (n\tau_{\mathrm{sc}}-3\sigma_m)^2/2\left(\sigma_{t,\mathrm{sc}}^2+\sigma_m^2\right)}. \tag{A.8}$$

Using the relation

$$\int_{-\infty}^{+\infty} e^{-(t-\mu)^2/2\sigma^2}\mathrm{d}t = \sqrt{2\pi}\sigma, \tag{A.9}$$

K can be written as

$$K = \sqrt{2\pi}\sigma_{tm}\sum_{n=1}^{N_{s,\mathrm{sc}}-1} e^{-(n\tau_{\mathrm{sc}}-3\sigma_m)^2/2\left(\sigma_{t,\mathrm{sc}}^2+\sigma_m^2\right)}. \tag{A.10}$$

Substituting (A.4), (A.5) and (A.10) into (A.8) yields the solution (10) presented in section 2.3.

ORCID iDs

K W A van Dongen https://orcid.org/0000-0001-6711-5898
D R Schaart https://orcid.org/0000-0002-3199-5608

References

Ahmad M, Xiang L, Yousefi S and Xing L 2015 Theoretical detection threshold of the proton-acoustic range verification technique *Med. Phys.* **42** 5744–53

Bakker J F, Paulides M M, Obdeijn I, van Rhoon G C and van Dongen K W A 2009 An ultrasound cylindrical phased-array for deep heating in the breast: theoretical design using heterogeneous models *Phys. Med. Biol.* **54** 3201–15

Bortfeld T 1997 An analytical approximation of the Bragg curve for therapeutic proton beams *Med. Phys.* **24** 2024–33

Bromiley P A 2018 Products and convolutions of Gaussian probability density functions

Favaudon V et al 2014 Ultrahigh dose-rate flash irradiation increases the differential response between normal and tumor tissue in mice Sci. Transl. Med. 6 245ra93
Fokkema J T and van den Berg P M 1993 Seismic Applications of Acoustic Reciprocity (Amsterdam: Elsevier)
Hayakawa Y, Tada J, Arai N, Hosono K, Sato M, Wagai T, Tsuji H and Tsuji H 1995 Acoustic pulse generated in a patient during treatment by pulsed proton radiation beam Radiat. Oncol. Invest. 3 42–5
Hickling S, Xiang L, Jones K C, Parodi K, Assmann W, Avery S, Hobson M and El Naqa I 2018 Ionizing radiation-induced acoustics for radiotherapy and diagnostic radiology applications Med. Phys. 45 e707–21
Jones K C, Vander Stappen F, Bawiec C R, Janssens G, Lewin P A, Prieels D, Solberg T D, Sehgal C M and Avery S 2015 Experimental observation of acoustic emissions generated by a pulsed proton beam from a hospital-based clinical cyclotron Med. Phys. 42 7090–7
Jones K C, Seghal C M and Avery S 2016 How proton pulse characteristics influence protoacoustic determination of proton-beam range: simulation studies Phys. Med. Biol. 61 2213–42
Jones K C, Nie W, Chu J C H, Turian J V, Kassaee A, Sehgal C M and Avery S 2018 Acoustic-based proton range verification in heterogeneous tissue: simulation studies Phys. Med. Biol. 63 025018
Kellnberger S, Assmann W, Lehrack S, Reinhardt S, Thirolf P, Queirós D, Sergiadis G, Dollinger G, Parodi K and Ntziachristos V 2016 Ionoacoustic tomography of the proton Bragg peak in combination with ultrasound and optoacoustic imaging Nat. Sci. Rep. 6 1–7
Krumholz A, Yao J, Wang L V, vanVickle-Chavez S J, Fleming T and Gillanders W E 2011 Photoacoustic microscopy of tyrosinase reporter gene in vivo J. Biom. Opt. 16 1–4
Lehrack S et al 2017 Submillimeter ionoacoustic range determination for protons in water at a clinical synchrocyclotron Phys. Med. Biol. 62 L20–30
Min C-H, Kim C H, Youn M-Y and Kim J-W 2006 Prompt gamma measurements for locating the dose falloff region in the proton therapy Appl. Phys. Lett. 89 183517
NIST 2018 PSTAR stopping-power and range tables for protons in water (https://physics.nist.gov/PhysRefData/Star/Text/PSTAR.html) retrieved on 01-08-2018 (National Institute of Standards and Technology)
Oraevsky A A and Karabutov A A 2000 Ultimate sensitivity of time-resolved optoacoustic detection Proc. SPIE 3916 228–39
Ozmen-Eryilmaz N, Demi L, Alles E J, Verweij M D and van Dongen K W A 2011 Modeling acoustic wave field propagation in 3D breast models IEEE Int. Ultrasonics Symp. (IEEE) pp 1700–3
Parodi K 2015 Vision 20/20: positron emission tomography in radiation therapy planning, delivery, and monitoring Med. Phys. 42 7153–68
Parodi K et al 2007 Patient study of in vivo verification of beam delivery and range, using positron emission tomography and computed tomography imaging after proton therapy Int. J. Radiat. Oncol. Biol. Phys. 68 920–34
Patch S K et al 2016 Thermoacoustic range verification using a clinical ultrasound array provides perfectly co-registered overlay of the Bragg peak onto an ultrasound image Phys. Med. Biol. 61 5621–38
Readhead M L 2014 Is underwater thermal noise useful? 43rd Int. Congress on Noise Control Engineering: Improving the World through Noise Control
Rosenthal A, Razansky D and Ntziachristos V 2010 Fast semi-analytical model-bases acoustic inversion for quantitative optoacoustic tomography IEEE Trans. Med. Imaging 29 1275–85
Schwaab J, Brons S, Fieres J and Parodi K 2011 Experimental characterization of lateral profiles of scanned proton and carbon ion pencil beams for improved beam models in ion therapy treatment planning Phys. Med. Biol. 56 7813–27
Sulak L et al 1979 Experimental studies of the acoustic signature of proton beams traversing fluid media Nucl. Instrum. Methods 161 203–17
Taskin U, Ozmen N, Gemmeke H and van Dongen K W A 2018 Modeling breast ultrasound; on the applicability of commonly made approximations Arch. Acoust. 43 425–35
Unkelbach J and Paganetti H 2018 Robust proton treatment planning: physical and biological optimization Semin. Radiat. Oncol. 28 88–96
van Dongen K W A, Brennan C and Wright W M D 2007 Reduced forward operator for electromagnetic wave scattering problems IET Sci. Meas. Technol. 1 57–62
van Dongen K W A, de Blécourt A J, Lens E, Schaart D R and Vos F M 2018 Modelling the iono-acoustic wave field for proton beam range verification IEEE Int. Ultrasonics Symp. pp 1–4
Verweij M D, Treeby B E, van Dongen K W A and Demi L 2014 Simulation of Ultrasound Fields (Amsterdam: Elsevier) pp 465–99
Wang L V 2008 Tutorial on photoacoustic microscopy and computed tomography IEEE J. Quantum Electron. 14 171–9
Winkler A M, Maslov K and Wang L V 2013 Noise-equivalent sensitivity of photoacoustics J. Biomed. Opt. 18 1–11
Xu M and Wang L V 2005 Universal back-projection algorithm for photoacoustic computed tomography Phys. Rev. E 71 016706
Yao D, Zhang C, Maslov K and Wang L V 2014 Photoacoustic measurement of the Grüneisen parameter of tissue J. Biomed. Opt. 19 1–8